

NeAS: 3D Reconstruction from X-ray Images using Neural Attenuation Surface

Chengrui Zhu¹, Ryoichi Ishikawa¹, Masataka Kagesawa¹, Tomohisa Yuzawa^{1,2}, Toru Watsuji², and Takeshi Oishi¹,

Abstract—Reconstructing three-dimensional (3D) structures from two-dimensional (2D) X-ray images is a valuable and efficient technique in medical applications that requires less radiation exposure than computed tomography scans. Recent approaches that use implicit neural representations have enabled the synthesis of novel views from sparse X-ray images. However, although image synthesis has improved the accuracy, the accuracy of surface shape estimation remains insufficient. Therefore, we propose a novel approach for reconstructing 3D scenes using a Neural Attenuation Surface (NeAS) that simultaneously captures the surface geometry and attenuation coefficient fields. NeAS incorporates a signed distance function (SDF), which defines the attenuation field and aids in extracting the 3D surface within the scene. We conducted experiments using simulated and authentic X-ray images, and the results demonstrated that NeAS could accurately extract 3D surfaces within a scene using only 2D X-ray images.

I. INTRODUCTION

Three-dimensional (3D) imaging of anatomical structures is helpful in clinical applications, such as diagnosis, surgery planning, and postoperative follow-up. The typical approach to obtain such 3D information is computed tomography (CT). CT provides 3D, high-resolution, and high-contrast images that help detect bone and blood vessel abnormalities, infections, tumors, and other symptoms. However, CT requires the capture of numerous slices or images to achieve high-resolution modeling, which exposes patients to high-level ionizing radiation.

Among the CT methods, cone beam CT (CBCT) offers a relatively low radiation dose, and enhancements have been made to the accuracy and resolution of 3D reconstruction [1]–[3]. There exists a trade-off among the number of images acquired and the performance of CBCT. Since acquiring fewer images inevitably introduces noise and artifacts into the reconstructed CT volume, mitigating these issues can help reduce radiation exposure. Consequently, extensive research in recent years has focused on integrating deep learning methods for CT reconstruction [4], [5].

Recent studies have employed implicit neural representations (INRs) to reconstruct CT volumes from sparse X-ray images [6]–[9]. Over the past several years, INRs such as neural radiance fields (NeRF) have gained popularity as a method for representing 3D scenes [10]–[12]. By

encoding scenes into the weights of neural networks via differentiable rendering techniques, INRs enable the high-precision reconstruction of 3D scenes with complex lighting and material properties. In the context of X-ray imaging, the neural attenuation field (NAF) allows for the estimation of the attenuation coefficient at each point [6]. Owing to its precise reconstruction capabilities, CT volumes can be generated from a relatively small number of images.

However, these INR-based methods do not accurately reconstruct the surface geometry of the objects in the scene. When extracting a surface from a CT volume, mesh data is produced from voxel values using techniques such as the Marching Cubes algorithm. If the volume lacks sufficient resolution, aliasing issues can arise. Moreover, since INR-based methods learn attenuation fields by maintaining consistency between the input and rendered images, the problem of 3D-2D ambiguity is unavoidable. This problem is particularly pronounced in X-ray imaging, where the visual perspective shifts significantly with changes in viewpoint.

Therefore, we introduced Neural Attenuation Surface (NeAS) to acquire accurate 3D shapes from X-ray images within the INR framework. NeAS utilizes the signed distance function (SDF) [13] to describe the target surface that bounds the neural attenuation fields. Because a single set of attenuation fields and an SDF cannot represent the boundary surfaces between several different materials, such as bones and muscles, we also proposed an architecture for cases involving multiple materials. In addition, since precisely calibrated systems are extremely costly, the proposed method employs a pose refinement approach to account for errors in extrinsic parameters.

The contributions of this paper can be summarized as follows:

- We propose an INR-based framework that integrates SDF and NAF by introducing the surface boundary function (SBF), enabling accurate 3D surface reconstruction from X-ray images.
- We also introduce an approach that simultaneously estimates multiple object surfaces, such as bone and skin, using multiple attenuation fields.
- We demonstrate that incorporating a robust pose refinement method with frequency regularization allows for more accurate estimation of attenuation and signed distance fields.

We further show that our approach enhances performance in a novel view synthesis task and successfully extracts surfaces

¹The authors are with The Institute of Industrial Science, The University of Tokyo, Japan. Emails: {zhucr, Ishikawa, kagesawa, yuzawa-tom, oishi}@cvl.iis.u-tokyo.ac.jp

²The authors are Air Water Inc., Minami Semba, Chuo-ku, Osaka, Japan. Emails: watsuji-tor@awi.co.jp

even in scenes containing multiple materials.

II. RELATED WORK

In this section, we begin with a brief review of previous studies on 3D surface reconstruction from X-ray images. Since CBCT has a long history and numerous survey papers have been published [1]–[5], we will focus on introducing surface estimation methods within the field of computer vision. Following this, we provide an explanation of INR methods relevant to this study and discuss INR-based 3D reconstruction from X-ray images.

A. 3D Surface Reconstruction from X-ray Images

Most traditional 3D reconstruction approaches rely on the deformation models [14]–[16]. These methods typically require 3D template models of the target, which are subsequently transformed based on input X-ray images. The statistical shape model (SSM) [17] [18] and statistical shape and intensity model (SSIM) [19] [20] are frequently employed to characterize such deformation models. These models establish statistical representations of the shape geometry and variances, resulting in a reduced number of parameters for optimization compared with general-purpose models.

The effectiveness of deep learning has been demonstrated in various tasks, including 3D reconstruction from X-ray images. CNN excels in object detection, and SSM is deformed using detected feature points and boundaries for 3D reconstruction [21], [22]. Hybrid deep neural network [23] that uses CNN for feature extraction and graph convolutional network (GCN) for model transformation has also shown good performance. Meanwhile, an end-to-end 3D reconstruction approach [24] eliminates the need for prior 3D knowledge, where the CNN directly outputs a 3D reconstruction model. GAN [25] can also be applied for 3D generation based on given 2D X-ray images. However, these methods often struggle with the absence of a prior model or a lack of training data.

B. Implicit Neural Representation

INR is a method for representing 3D scenes with neural networks, as opposed to explicit representations, such as point clouds and triangle meshes. NeRF [10] demonstrated promising results in novel view synthesis by optimizing a neural network through ray sampling and volume rendering. However, the original NeRF faces challenges such as slow training and inference speeds. Additionally, NeRF requires a substantial number of images, such as several hundred images, to achieve sufficient quality in the synthesized images, posing a significant limitation.

Recently, more research has attempted to overcome these limitations of the NeRF. The remainder of this section describes methods for improving the NeRF that are related to the proposed method.

1) *Acceleration*: Various methods are aimed at improving NeRF’s training speed. The general approach involves storing 3D feature embeddings in an explicit spatial structure combined with a compact decoder network to query the density

and color of a sampled point. Point-NeRF [26] adopts a point cloud to embed points, whereas TensorRF [27] uses a voxel grid with low-rank decomposition. Instant-NGP [28] implements a multiresolution hash map, which significantly reduces the memory requirements of the grid representation. Plenoxels [29] innovatively eliminates the decoder network and acquires color directly from the spherical harmonics. The proposed method also uses hash encoding to query sampled points.

2) *Geometry-centric approach*: Although NeRF excels in rendering high-quality 2D images, it struggles to reconstruct the 3D geometry accurately. Thus, recent efforts have focused on enhancing the geometric consistency of surfaces within a scene. For instance, UniSurf [30] simultaneously learns implicit surfaces and NeRFs using an occupancy field to represent the surfaces. Meanwhile, NeuS [13] employs implicit surfaces and represents them using an SDF. SDF is utilized in the volume-rendering process and enables the extraction of surfaces at their zero-level sets. NeuS2 [31] employs hash encoding to accelerate the training and inference processes and to extend the representation capability to dynamic scenes. Our work also incorporates SDF for surface learning, but uniquely applies it to X-ray images, differing from the approach used for RGB images.

3) *Pose refinement*: Accurate camera parameters are crucial for successful implementation of NeRF. Therefore, several studies have focused on optimizing the camera parameters while training the NeRF. For example, BARF [32] introduced a coarse-to-fine strategy for positional encoding of camera poses. Meanwhile, SCNeRF [33] implemented geometric loss to enhance the optimization of camera poses and lens distortion. GRAF [34] learned poses from a random distribution. NoPe-NeRF [35] utilized mono-depth maps to simultaneously constrain relative frame poses and regularize NeRF’s geometry.

To mitigate inaccurate camera parameters when taking X-ray photographs, our work also incorporates pose refinement during training and optimizes the camera parameters concurrently with the attenuation field.

C. INR-Based X-Ray Imaging

Several studies used implicit representations for CT volume reconstruction. For instance, NAF [6] learns a neural attenuation field for CBCT reconstruction using a hash encoder similar to that in [28] for efficient training. Meanwhile, SNAF [8] integrates a deblurring network to address the sparse-view problem inherent in NAF. NeAT [7] uses an octree grid structure to store 3D feature embeddings coupled with a compact multilayer perceptron (MLP) for decoding. SAX-NeRF uses Transformer to enable the recovery of detailed structural information during CT reconstruction [9].

As mentioned above, these approaches face challenges in accurately reconstructing 3D surface geometries. This is similar to the scenario seen between NeRF and geometry-centric methods such as NeuS [13], [31] in the visible spectrum. Therefore, we designed a framework to extract

surfaces and enhance geometric consistency in the neural attenuation field.

III. METHOD

We adopt an implicit neural modeling approach to reconstruct 3D scenes with X-ray images. Fig. 1 provides an overview of our method termed NeAS. Given a set of input X-ray images $\mathcal{I}^X = \{I_i\} (i = 1, 2, \dots, n^X)$, our method constructs attenuation fields $\Theta_{\text{att}*}$ and an implicit SDF Θ_{sdf} . n^X is the number of input images. The attenuation field determines the attenuation coefficient at each point within the scene, whereas the SDF continuously represents the surface, providing a detailed and continuous geometric description. The trained SDF offers a 3D geometric constraint to the attenuation field.

A. Neural Attenuation Surface

1) *Overview*: Let us begin by considering only one concerning surface: the object–air surface. Here, we assumed that the attenuation of the signal in air is sufficiently small to be distinguishable from that of the object. We assumed that the initial parameters of the intrinsic and extrinsic parameters (\mathbf{K}, \mathbf{p}_i) of the input image I_i are given by calibration. The detail of the projection model and the pose refinement are described in Section III-C. We represented a scene with MLPs: an attenuation field Θ_{att} and an SDF Θ_{sdf} (Fig. 1).

We sampled a 3D point $\mathbf{x} \in \mathbb{R}^3$ along a ray $\mathbf{r} \in \mathbb{R}^3$ corresponding to a pixel $\mathbf{u} \in \mathbb{R}^2$ in an X-ray frame: $\mathbf{x} = \mathbf{o} + t\mathbf{r}$. Here, t is the travel distance from the origin \mathbf{o} to the sampled point. We omitted the indices for simplicity. The input to Θ_{sdf} is the encoded position, $\Gamma(\mathbf{x})$, where $\Gamma(\cdot)$ is a positional encoding function. The output of Θ_{sdf} is the intermediate K -dimensional feature vector $\mathbf{f} \in \mathbb{R}^K$ and signed distance $d \in \mathbb{R}$. \mathbf{f} is the input of the attenuation field Θ_{att} . We applied a surface-bound function $\Omega(d, s)$ to the obtained signed distance with a learnable parameter $s \in \mathbb{R}$ to retain the attenuation only inside the surface. Finally, the network outputs the attenuation coefficient at \mathbf{x} as $\mu(\mathbf{x})$ by multiplying the bounded signed distance by the attenuation factor $\bar{\mu}$, which is the output of Θ_{att} .

The method obtains the pixel intensity corresponding to a ray with all sampled points through volume rendering and compares the intensity with the ground truth. The detail of the rendering model is described in III-A.5. We applied a ray-casting approach [36] to calculate the rays’ transmittance as they traveled through the scene during volume rendering. The backpropagation process optimized Θ_{sdf} and Θ_{att} . The following sections explain the key functions of this framework.

2) *Sampling and encoding*: We employed a stratified method [10] to sample the 3D points along a ray within a fixed range. The stratified sampling method divided the points into several mutually exclusive and inclusive “strata” and randomly sampled from each stratum. Note that we did not use a hierarchical sampling strategy because it was not suitable for X-ray conditions, where each point along the

ray contributed uniformly, unlike in RGB images, where the points closer to the surface have major contributions.

We applied positional encoding methods, which encoded the input position into a higher-dimensional space to enable the learning of high-frequency variations in intensity and geometry. The encoding approach addressed the MLP’s inclination toward lower frequency functions [37]. We implemented two encoding techniques: frequency encoding [10] and hash encoding [28].

Frequency encoding involves the use of sine and cosine functions to facilitate high-dimensional mapping, as utilized in the original NeRF. A mapping function γ maps the input value $p \in \mathbf{x}$ from \mathbb{R} to \mathbb{R}^{2L} :

$$\gamma(p) = (\sin(2^0\pi p), \cos(2^0\pi p), \dots, \sin(2^{L-1}\pi p), \cos(2^{L-1}\pi p)), \quad (1)$$

where L determines the highest frequency.

Hash encoding leverages a multiresolution voxel grid structure to store feature embeddings with a hash table, which significantly reduces memory requirements for maintaining this lookup table. The detailed implementation is the same as that of Instant-NGP [28].

3) *Surface boundary function*: SDF predictions were utilized to establish a surface boundary function (SBF) that could further modify the attenuation coefficient obtained from Θ_{att} . As depicted in Fig. 2, for an arbitrary ray, the ray intersects the object surfaces twice, indicating surface boundaries at these points. We defined the SBF by resembling a sigmoid function as follows:

$$\Omega(d, s) = \frac{\exp(-sd)}{1 + \exp(-sd)}, \quad (2)$$

where s is a learnable parameter governing the steepness of the surface boundaries. The variation of the boundary function with parameter s is shown in Fig. 2.

Ideally, the SBF should be a unit step function equal to 1 inside the object and 0 outside, so that only the attenuation within the object’s surface is preserved (see also Eq. (3)), effectively disregarding the external attenuation. However, the step function has challenges in terms of gradient propagation during training. To address this, we approximated the step function with a sigmoid function, which closely resembled the desired behavior and facilitated smoother gradient propagation, thereby enhancing the model’s learning efficiency.

4) *Neural attenuation field*: By using the vector \mathbf{f} output from Θ_{sdf} as the input, Θ_{att} outputs the attenuation parameter $\bar{\mu} \in \mathbb{R}$. By applying the SBF (Eq. (2)) to the parameter, we obtained the detailed attenuation coefficient $\mu \in \mathbb{R}$ at the sampled point \mathbf{x} as follows:

$$\mu(\mathbf{x}) = \Omega(d, s)\bar{\mu}. \quad (3)$$

Θ_{att} must produce an output $\bar{\mu} > 0$ to retain attenuation only within the interior of the surface. Therefore, we employed the activation function $\alpha\sigma(x) + \beta$ in the last layer of Θ_{att} . Here, $\sigma(\cdot)$ denotes the sigmoid function and $\alpha(> 0) \in \mathbb{R}$ and $\beta(> 0) \in \mathbb{R}$ are parameters that are adjusted

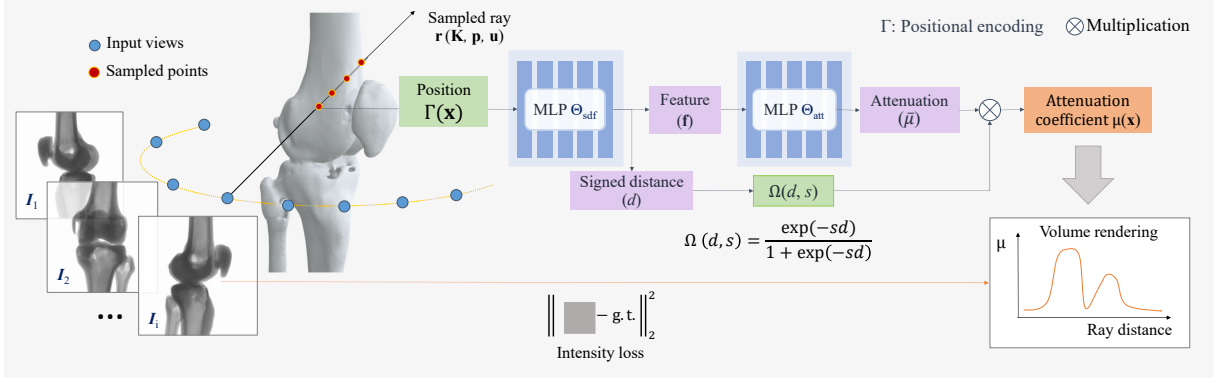


Fig. 1. Overview of our framework. To render a pixel of an image, first sample 3D points along the corresponding ray, and then query the SDF and attenuation coefficient of these points using MLP Θ_{sdf} and Θ_{att} . A surface-bound function was calculated from the SDF and used to constrain attenuation, retaining the attenuation only inside the surface. Then, attenuations are accumulated for volume rendering. The final pixel intensity is compared with the ground truth by MSE loss, which is backpropagated to optimize MLPs.

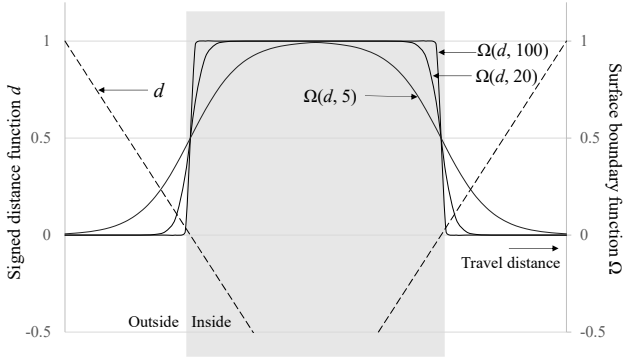


Fig. 2. Surface boundary function (SBF) $\Omega(d, s)$ with SDF values d on a certain ray and different s parameters. As the s value increases, the more accurate the surface position is determined.

based on the attenuation characteristics of the object. Thus, the range of the attenuation parameter $\bar{\mu}$ was $[\beta, \beta + \alpha]$. β determines the minimum attenuation value and ensures that it is not zero. This constraint is crucial because only the SBF is designed to determine the regions of nonzero attenuation (where the signed distance $d < 0$) and areas with zero attenuation (where $d > 0$). If β were set to zero, the final attenuation coefficient $\mu(\mathbf{x})$ could be 0 when $\bar{\mu} = 0$ even in regions where $d < 0$. In such cases, the SBF cannot represent accurate boundaries.

5) *Rendering and optimization:* Once the attenuation coefficients for all points along a ray were determined, we calculated the pixel intensity corresponding to the ray using volume rendering. Since X-rays are generally absorbed without being scattered by most materials, Lambert-Beer's law is assumed to hold.

If the attenuation coefficient μ is a continuous function of the distance t , the observed light intensity $\hat{I}(\mathbf{r})$ after traveling a distance T can be written as follows:

$$\hat{I}(\mathbf{r}) = I_0(\mathbf{r}) \int_0^T \exp(-\mu(t)) dt, \quad (4)$$

where $I_0(\mathbf{r})$ is the light intensity emitted from the X-ray source to the ray direction $-\mathbf{r}$.

Assuming that the attenuation in the air is sufficiently small, I_0 can be regarded as the maximum pixel value: $I_0 = 1$. By applying the quadrature rule [38], we can approximate the calculation of the integral while maintaining differentiability for optimization purposes:

$$\hat{I}(\mathbf{r}) = \exp(-\sum_{i=j}^N \mu(\mathbf{x}_j) \delta_j), \quad (5)$$

where δ_j is the adjacent distance between t_{j+1} and t_j and N is the total number of sampled points on the ray \mathbf{r} .

Finally, the predicted ray intensity $\hat{I}(\mathbf{r})$ is compared with the input pixel intensity by calculating the MSE loss:

$$\mathcal{L}_{\text{int}} = \sum_{\mathbf{r} \in \mathcal{R}} \|\hat{I}(\mathbf{r}) - I(\mathbf{r})\|_2^2, \quad (6)$$

where \mathcal{R} is a sampled batch of the rays. We applied an Eikonal term [39] to regularize SDF as follows:

$$\mathcal{L}_{\text{reg}} = \frac{1}{mn} \sum_{k,j} (\|\mathbf{n}_{k,j}\| - 1)^2. \quad (7)$$

where m is the batch size, n is the point sampling size, and \mathbf{n} is the gradient of the SDF field at the sampling point. Then, the final loss for the optimization is calculated as follows:

$$\mathcal{L} = \mathcal{L}_{\text{int}} + \lambda \mathcal{L}_{\text{reg}}, \quad (8)$$

where λ is a weighting parameter.

B. NeAS for Multiple Materials

In the case of the human body, the boundaries between multiple materials must be distinguished. For example, as illustrated in Fig. 4, an X-ray image of the leg, in addition to the outer skin-air surface, shows that the internal bone-muscle surface is also prominently visible. The approach outlined in the previous section was designed to extract only the surfaces of one material. Therefore, we proposed NeAS for two materials (2M-NeAS) with different attenuation coefficients.

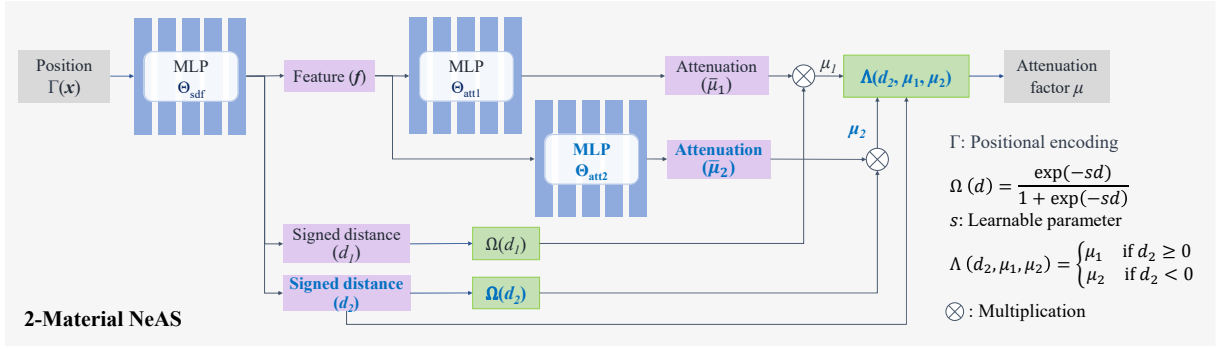


Fig. 3. Pipeline to query attenuation coefficient for two materials.

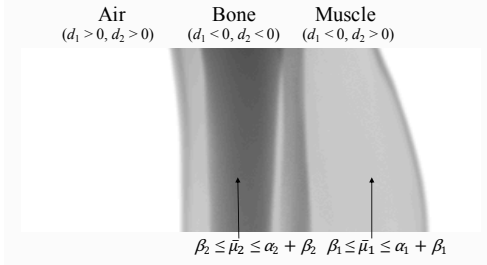


Fig. 4. Brief illustration of the attenuation coefficient in a bone and muscle area.

1) *Framework*: 2M-NeAS represents two signed distance functions using one MLP Θ_{sdf} , and the attenuation fields using independent MLPs Θ_{att1} and Θ_{att2} for each field. Fig. III-A.1 shows the pipeline of the proposed method. Θ_{sdf} models two SDFs and outputs the signed distances for both materials in addition to the intermediate feature vectors $d_1 \in \mathbb{R}$, $d_2 \in \mathbb{R}$ and $\mathbf{f} \in \mathbb{R}^K$. For example, d_1 represents the skin–air surface, whereas d_2 represents the bone–muscle surface.

We assigned two separate MLPs for the two attenuation fields. If we used only one MLP for the attenuation fields, a point near the boundary of two materials would be influenced by both fields. Modifications to the SDF during training would cause the boundary to shift continuously. Consequently, the output of the MLP at these points would exhibit significant fluctuations. Therefore, we added an MLP to represent another attenuation field. Θ_{att1} and Θ_{att2} are attenuation fields to predict the attenuation parameters $\bar{\mu}_1$ and $\bar{\mu}_2$, respectively. We applied Eq. (3) and then obtained the attenuation coefficients as $\mu_1 = \Omega(d_1, s)\bar{\mu}_1$ and $\mu_2 = \Omega(d_2, s)\bar{\mu}_2$.

The activation function for Θ_{att1} and Θ_{att2} is $\alpha\sigma(x) + \beta$. Thus, the value ranges of $\bar{\mu}_1$ and $\bar{\mu}_2$ differ: $(\beta_1, \alpha_1 + \beta_1)$ and $(\beta_2, \alpha_2 + \beta_2)$. Tailoring these parameters to the specific characteristics of the materials being imaged is crucial to ensure that the ranges of muscle and bone attenuation do not overlap. Nonoverlapping ranges are essential for maintaining the distinctiveness of SDFs in accurately representing respective surfaces.

2) *Selecting function*: Because the proposed framework generates two attenuation coefficients μ_1 and μ_2 , we must select the proper one for the point \mathbf{x} . Therefore, we introduce a selector mechanism to determine which of the two attenuation values may be chosen as the final prediction as follows:

$$\mu = \Lambda(d_2, \mu_1, \mu_2) = \begin{cases} \mu_1 & (d_2 \geq 0) \\ \mu_2 & (d_2 < 0) \end{cases} \quad (9)$$

This approach implies the following: if this point lies inside the bone where $d_2 < 0$, we output μ_2 as the final attenuation; if this point belongs to the muscle, μ_1 is output instead. This distinction is dynamic and may evolve as the SDFs are optimized during the training process. Fig. 4 presents a conceptual visualization of the leg-part X-ray image. The bone is surrounded by muscle, and $d_2 < 0$, the final attenuation should be μ_2 . Outside the bone, where $d_2 \geq 0$, everything is the same as in Section III-A.

C. Pose Refinement

Because accurate projection parameters are essential for traversing the ray, we optimized and refined the poses of the X-ray source and flat panel detector (FPD). In an X-ray imaging system using robotic arms or a turntable, even after calibration, we cannot avoid residual errors in the poses of the X-ray source and FPD relative to the target. Therefore, we refined the poses for all input X-ray images simultaneously while training the NeAS. The entire rendering process was differentiable, which allowed the loss to backpropagate and adjust the camera poses, enabling concurrent optimization along with network parameters.

1) *Camera model*: The X-ray system can be regarded as a pinhole camera system, where the X-ray source functions as the optical center, and the FPD serves as the image plane. The measurement system did not include lenses; therefore, we did not consider lens distortion. Our focus in pose refinement was primarily on the uncertainties in the object–source distance and source–panel relative position. Consequently, we optimized only the translation components in the extrinsic parameters and principal points in the intrinsic parameters. Here, we assumed that reasonable initial parameters are given.

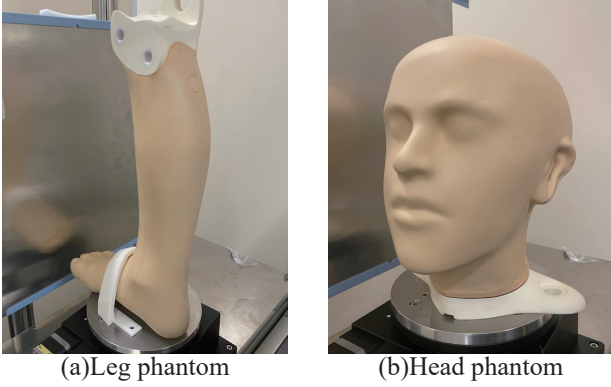


Fig. 5. Phantoms used for X-ray image capturing.

2) *Coarse-to-fine strategy*: In X-ray imaging, not only the surface point contributes to the final pixel value, and the inner points along the ray also play important roles. That is, even minor changes in the viewing angle can lead to substantial changes in the rendering results, as all points along a given ray can shift drastically. In other words, refining poses using a gradient-based approach by back-propagation is challenging.

To address this problem, we incorporated a frequency regularization approach by integrating a weight mask into the encoding process, as has been done previously [31], [40], [41]. Frequency regularization has also been proven to be effective in grid-based feature encoding [42]. At the beginning of the training, we were only concerned with low-frequency outlines, and the rendering results were predominantly derived from the lower-frequency part of the input. As training progressed, high-frequency features were utilized. The mask reweighted the components in the k th frequency as follows:

$$\hat{\Gamma}_k(p) = w_k(\tau)\Gamma_k(p), \quad (10)$$

where Γ_k can be the frequency encoding at frequency k or hash encoding at the k th resolution. w_k is defined as

$$w_k(\tau) = \begin{cases} 0 & \tau < k \\ \frac{1 - \cos((\tau - k)\pi)}{2} & 0 \leq \tau - k < 1 \\ 1 & \tau - k \geq 1, \end{cases} \quad (11)$$

where τ is a parameter that increases in relation to the number of iterations during training. We also took a warming-up strategy; the pose refinement started after M ($=500$ in the experiment) iterations to avoid the early overfitting problem.

IV. EXPERIMENTAL RESULTS

A. Dataset

We conducted experiments using simulated and real X-ray images. We employed gVirtualXray [43] to obtain the simulated X-ray images. We generated 36 images of size

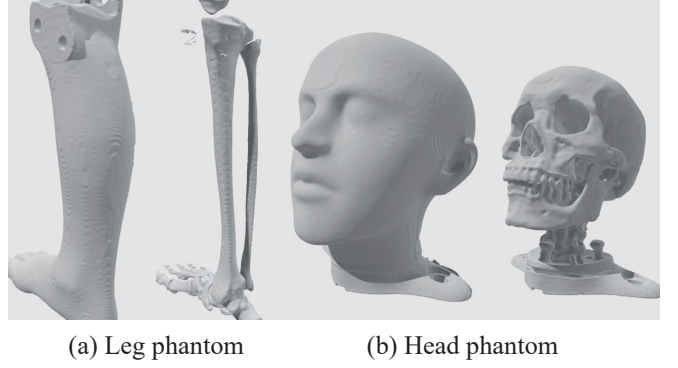


Fig. 6. 3D meshes of phantoms skin and bone extracted by Helical CT system

480×480 around the 3D models of the knee bone¹ and skull² derived from CT scans, altering the view direction by 10° . The trajectory of the X-ray source position is a circle on the x - y plane. From a total of 36 images, five were selected for validation purposes, and the model was trained using the remaining 31 images. The distance from the source to the object's center was 40 cm, whereas that from the center of the object to the detector panel was 10 cm.

We captured 30 real images around a phantom using a computer-controlled turntable panel, with a 12° change in the angle for each image. Phantoms include a leg and a head phantom as shown in Fig. 5. Fig. 6 shows the 3D meshes of the phantoms bone and skin obtained by Helical CT scan using Aquilion Prime SP provided by Canon Medical Systems. Out of 30 views, four images were designated as validation images, whereas the remainder were used for training. The distance between the source and FPD was approximately 1 m, whereas the distance from the X-ray source to the object was approximately 77 cm. Note that these distances were not exact, resulting in inaccuracies in the camera parameters. Pose refinement was used to compensate for these inaccuracies. The X-ray source voltage was set at 60 kV, and the current was set at 200 mA, ensuring that the images were relatively clear and minimally affected by noise.

B. Implementation Details

We assumed that the region of interest lies within a unit sphere; accordingly, the scene was initially scaled to fit within this sphere. Image pixel values were normalized to the range of $[0, 1]$, with the background set to 1 where the rays did not undergo attenuation. In each batch, 512 rays were randomly sampled and 128 points were sampled along each ray. For frequency encoding, Θ_{sdf} comprised six layers, each with a hidden size of 256, whereas Θ_{att} included three

¹embodi3d. (2017). Right knee - Bone model [3D model]. Retrieved from <https://www.embodi3d.com/files/file/12503-right-knee-bone-model-stl-file-from-converted-ct-scan/> (Licensed under CC)

²jagake. (2022). JAGAKE Full Skull [3D model]. Sketchfab. Retrieved from <https://sketchfab.com/3d-models/jagake-full-skull-a69cb39385ae4cbbad7962a816fd8c06> (Licensed under CC Attribution)

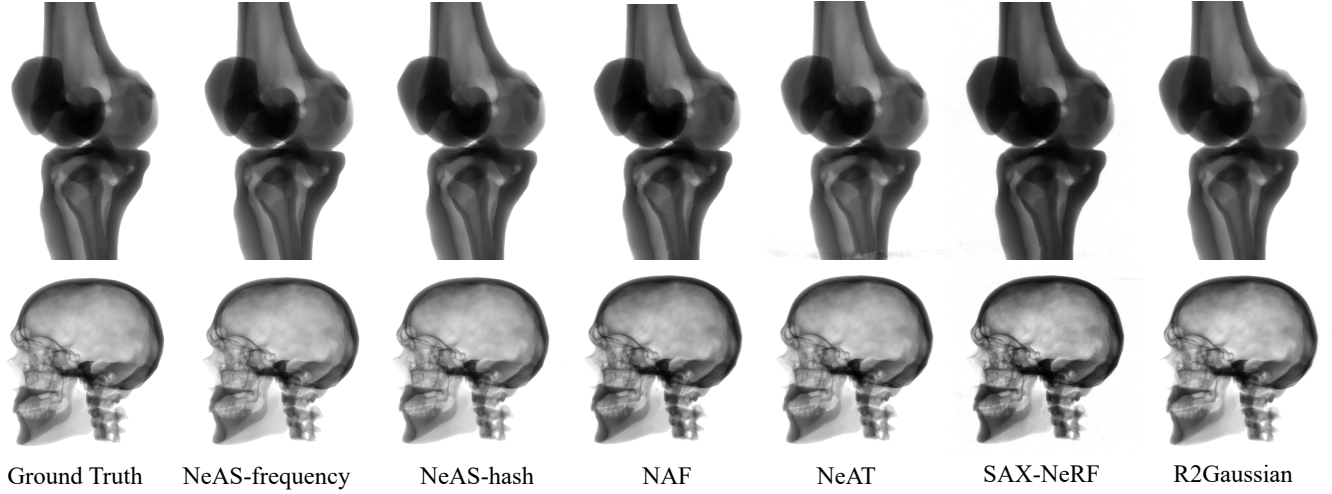


Fig. 7. Validation views for simulation dataset.

hidden layers, with a size of 256. For hash encoding, both Θ_{sdf} and Θ_{att} were constructed with two layers, each with a hidden size of 64. The resolution of hash encoding varied across the 14 levels, ranging from 16 to 2048.

For pose refinement, the parameter τ was first set to 2, so that the first two low-frequency components were of concern at the beginning. It then grew linearly to the largest frequency L until half of the total number of training iterations. Parameter s for the SBF was initialized as 20. For the 2M-NeAS experiment, we chose $\beta_1 = 0.1$, $\alpha_1 = 3.4$, $\beta_2 = 3.5$, and $\alpha_2 = 5.5$. The experiments were conducted using a single NVIDIA RTX3090 GPU.

Determining α and β : The parameters α and β are related to the attenuation coefficients of the target objects. If we can approximate μ_{air} , μ_{muscle} , and μ_{bone} , we can set two thresholds as follows:

$$t_1 = (\mu_{\text{air}} + \mu_{\text{muscle}})/2 \quad (12)$$

$$t_2 = (\mu_{\text{muscle}} + \mu_{\text{bone}})/2 \quad (13)$$

For the muscle, we can set the attenuation range as $[t_1, t_2]$ as follows:

$$\beta_1 = t_1 \quad (14)$$

$$\alpha_1 = t_2 - t_1. \quad (15)$$

For the bone, the attenuation range could be $[t_2, t_{\text{max}}]$, and t_{max} must be larger than the attenuation coefficients of all bone regions:

$$\beta_2 = t_2 \quad (16)$$

$$\alpha_2 = t_{\text{max}} - t_2. \quad (17)$$

Another method is to run a 1M-NeAS first and set a relatively large range for the attenuation coefficients. By analyzing the attenuation distribution, we can easily find the threshold values.

TABLE I
QUANTITATIVE COMPARISON ON KNEE SIMULATION DATA (AVERAGE OF FIVE VALIDATION VIEWS)

	PSNR \uparrow	SSIM \uparrow	LPIPS \downarrow	CD (mm) \downarrow
NeAS frequency	53.20	0.9996	0.0017	0.1877
NeAS hash	52.71	0.9995	0.0027	0.1462
NAF [6]	44.49	0.9974	0.0441	0.6082
NeAT [7]	48.37	0.9954	0.0424	0.2244
SAX-NeRF [9]	42.56	0.9824	0.0064	0.2432
R ² -Gaussian [44]	47.12	0.9970	0.0095	0.4021

TABLE II
QUANTITATIVE COMPARISON ON SKULL SIMULATION DATA (AVERAGE OF FIVE VALIDATION VIEWS)

	PSNR \uparrow	SSIM \uparrow	LPIPS \downarrow	CD (mm) \downarrow
NeAS frequency	48.35	0.9985	0.0063	0.3521
NeAS hash	49.29	0.9986	0.0186	0.167
NAF [6]	40.43	0.9877	0.0993	0.7390
NeAT [7]	46.59	0.9931	0.0655	0.3640
SAX-NeRF [9]	32.34	0.9082	0.1646	0.2871
R ² -Gaussian [44]	32.80	0.9333	0.1415	0.3855

C. Results on Simulation Data

We first evaluated the performance of our NeAS method on simulation data. There was only one surface of concern, so we utilized 1M-NeAS for this experiment. We used known camera poses to render the simulated images. We tested our NeAS in the knee-bone scene with frequency encoding and hash encoding.

1) Novel view synthesis: Figs. IV-A shows the synthesis results for validation views of knee and skull bones, alongside comparisons with NAF [6], NeAT [7], SAX-NeRF [9], and R²-gaussian [44]. The 2D results from NAF and NeAT appeared to fail to similarly have high quality at first glance. However, upon closer inspection, the results of NAF, NeAT, and SAX-NeRF seem to emphasize darker regions, indicating that the attenuation is estimated to be higher than correct

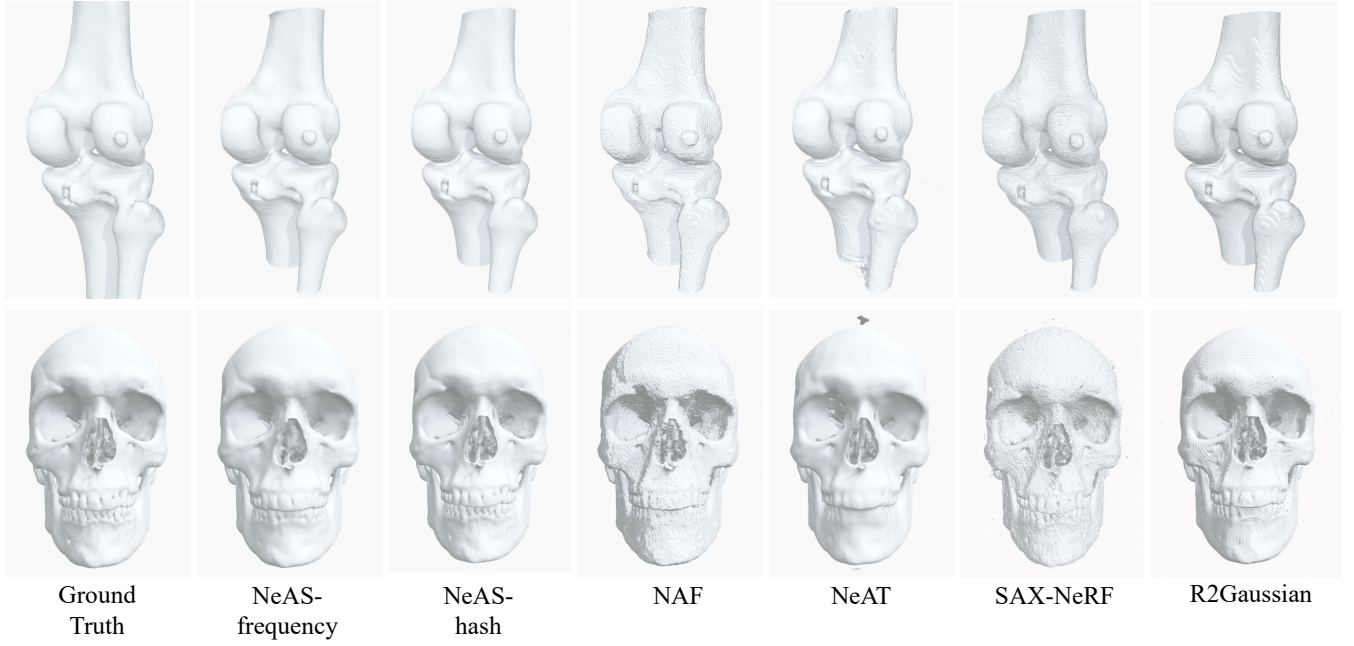


Fig. 8. Extracted knee-bone and skull surfaces. Note that reconstructed knee-bone models are partly included because of cone-beam imaging.

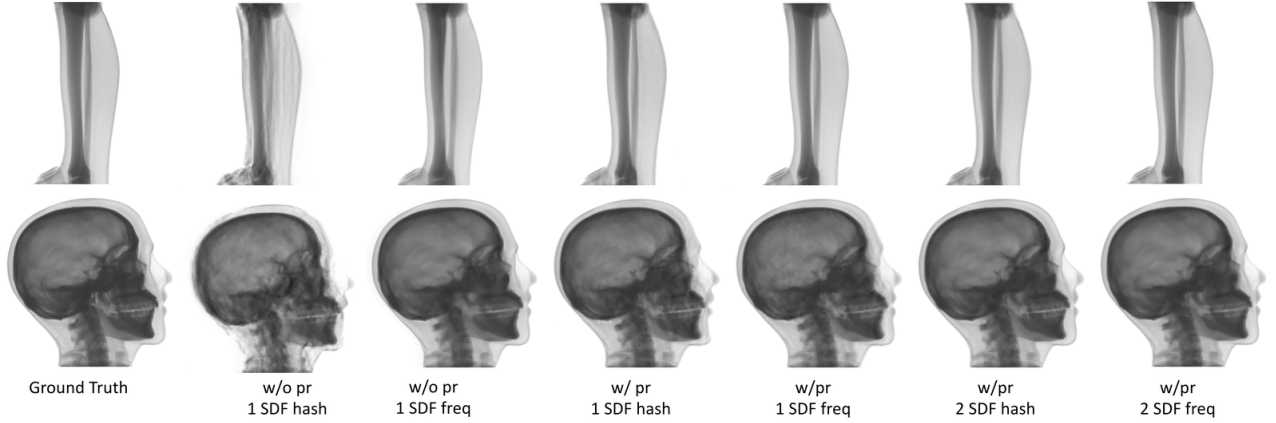


Fig. 9. 2D validation views for real leg and head X-ray image data. The results are compared with and without pose refinement, between hash encoding and frequency encoding, and between a 1 SDF setting and 2 SDF setting.

values. The results of the SAX-NeRF show the artifacts in the area other than the object.

A detailed quantitative comparison is shown in Tables I and II. The values are the average of five validation views. In the tables, Peak Signal-to-Noise Ratio (PSNR), Structural Similarity Index Measure (SSIM), and Learned Perceptual Image Patch Similarity (LPIPS) are metrics used to evaluate image similarities with the ground truth. The results revealed that NeAS provided superior performance in comparison to the other methods.

Meanwhile, the results of frequency encoding and hash encoding showed that their performances were nearly the same. However, the training speed for hash encoding was about 3.5 times that of frequency encoding.

2) Surface reconstruction: Qualitative evaluation: Figs. IV-B shows the results of the surface extraction of knee and skull bones, achieved by locating the zero-level set of SDF. The figures also show the surfaces extracted by NAF, NeAT, SAX-NeRF, and R²-Gaussian for comparison. We extracted the surface models of NAF, NeAT, and SAX-NeRF by manually setting the optimal density values and applying the Marching Cubes algorithm. The results prove that our method successfully reconstructed the surfaces accurately and smoothly.

Meanwhile, noticeable artifacts were evident on the surface of the NAF, suggesting that this method has difficulty reconstructing 3D geometry and surface, although it performs well in novel view synthesis. In comparison, although NeAT’s result appears reasonable, an artifact was discovered

at the top of the skull, and the reconstruction of the teeth still requires improvement.

Quantitative evaluation: We also evaluated the results quantitatively using the Chamfer distance (CD) by comparing them with the ground truth. As indicated in Tables I and II, our method outperformed the other approaches. Although NeAS with frequency encoding achieved better 2D results, hash encoding outperformed significantly in terms of the CD. We found that the surface extracted by the NeAS frequency was over-smoothed, and that some details were ignored. This may be attributed to the inherent bias of both Θ_{sdf} and Θ_{att} toward low-frequency features. The impact of this issue was less obvious in the knee-bone results, as they lacked significant high-frequency details, whereas the skull contained many high-frequency details. Conversely, the implementation of hash encoding significantly alleviated this problem. The multiresolution structure of hash encoding played an extremely important role, with higher-resolution voxel grids focusing on high-frequency details.

D. Results on Real Data

We performed experiments on real data taken from leg and head phantoms with 1M-NeAS and 2M-NeAS. Because precise camera parameters were not available, we turned to pose refinement. We first implemented pose refinement with all images including validation images. Then, fixing the refined camera parameters, we excluded validation images and trained the model solely on training images from the start. In this way, we can evaluate the results of the validation images quantitatively.

1) *Novel view synthesis:* Fig. 9 shows the validation images, and Table III presents the quantitative evaluation results. A comparison of the results with and without pose refinement indicated that pose refinement significantly enhanced the results qualitatively and quantitatively. This improvement was particularly notable in hash encoding experiments, where imprecise camera parameters could severely degrade the results. The comparison between 1M-NeAS and 2M-NeAS revealed no significant performance drop with the use of two SDFs and attenuation fields.

2) *Surface reconstruction:* **Qualitative evaluation:** In the meantime, we could extract the inner surface by learning two SDFs, as shown in Fig. 10. Here, we only show the results with pose refinement. Qualitative observations indicated that hash encoding faced difficulties with real data. The reconstructed surfaces appeared rough, and numerous nonexistent points were likely due to hash collisions or noise. In contrast, frequency encoding was more successful in learning smooth and accurate surfaces, producing results that closely resembled actual objects. However, the tendency of frequency encoding to generate relatively over-smoothed surfaces persisted. This was evident in the missing teeth gaps, whereas hash encoding was better in this regard.

Our observations highlight the need for a balanced approach to encoding techniques, particularly when dealing with intricate details in 3D reconstructions from X-ray images.

Quantitative evaluation: Table IV shows CD from point clouds extracted from volume data obtained by Helical CT scan using Aquilion Prime SP provided by Canon Medical Systems, on the real phantoms. (See Fig. 6) We used the segmentation module [45] implemented in 3D Slicer [46] for extracting the point cloud. We first aligned the two point clouds using the iterative closest point algorithm with optimizing scale [47] and then calculated the CD.

The results of the skin surface recovery using hash encoding showed that the CD increased due to the noise points inside the surface. Regarding the surface recovery of the bone, the results of the extraction using frequency encoding tended to be thicker than the extraction using the reference point group or hash encoding, and the CD value also increased accordingly. As the resolution of the volume data from the CT is 1 mm, it is difficult to make a precise accuracy comparison. However, the proposed method achieves surface reconstruction with no significant errors compared to the results from the helical CT.

V. CONCLUSION

We proposed NeAS, a novel method to reconstruct 3D surfaces from X-ray images and to synthesize X-ray images in new views. NeAS leveraged a combination of signed distance functions and neural attenuation fields. The SDF played a role in constraining the attenuation coefficient according to the boundaries of different materials. We introduced a surface-bound function derived from SDF to adjust the learned attenuation coefficient. Considering that camera parameters in real scenes may not always be precise, we implemented a coarse-to-fine strategy for intrinsic and extrinsic parameter refinement. We also incorporated hash-encoding to accelerate the training and inference processes, revealing its potential in capturing high-frequency details on surfaces. Furthermore, we demonstrated that our method provides an accessible alternative for bone density estimation using the predicted attenuation fields.

The major limitation of our method is the need for manual setting of α and β to determine the ranges of the attenuation values. Future studies should focus on developing an adaptive approach to determine these parameters. We also believe that expanding the proposed method to accommodate three or more materials would be beneficial.

REFERENCES

- [1] A. W. Yeung, R. Jacobs, and M. M. Bornstein, "Novel low-dose protocols using cone beam computed tomography in dental medicine: a review focusing on indications, limitations, and future possibilities," *Clinical oral investigations*, vol. 23, pp. 2573–2581, 2019.
- [2] P. Alaei and E. Spezi, "Imaging dose from cone beam computed tomography in radiation therapy," *Physica Medica*, vol. 31, no. 7, pp. 647–658, 2015.
- [3] H. Liu, D. Schaal, H. Curry, R. Clark, A. Magliari, P. Kupelian, D. Khuntia, and S. Beriwal, "Review of cone beam computed tomography based online adaptive radiotherapy: current trend and future direction," *Radiation Oncology*, vol. 18, no. 1, p. 144, 2023.
- [4] A. Biguri and S. Mukherjee, "Advancing the frontiers of deep learning for low-dose 3d cone-beam computed tomography (ct) reconstruction," in *2024 IEEE International Conference on Acoustics, Speech, and Signal Processing Workshops (ICASSPW)*. IEEE, 2024, pp. 81–82.

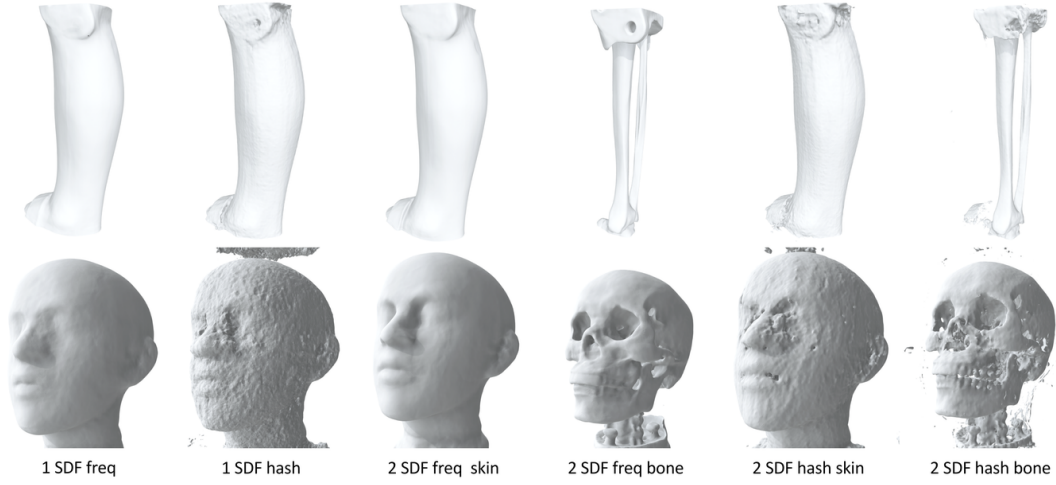


Fig. 10. 3D surfaces extracted from real X-ray data. Both 1 SDF and 2 SDF models were implemented. All the results were obtained from refined poses.

TABLE III
QUANTITATIVE RESULTS ON A REAL X-RAY DATASET.

Scene	Evaluation	w/o pr 1 SDF hash	w/o pr 1 SDF freq	w/ pr 1 SDF hash	w/ pr 1 SDF freq	w/ pr 2 SDF hash	w/ pr 2 SDF freq
Leg	PSNR↑	27.19	31.35	35.89	42.80	36.04	42.40
	SSIM↑	0.9325	0.9715	0.9861	0.9977	0.9854	0.9972
	LPIPS↓	0.1629	0.0701	0.0555	0.0216	0.0624	0.0236
Head	PSNR↑	26.69	33.81	32.30	37.05	32.72	36.38
	SSIM↑	0.9139	0.9763	0.9674	0.9880	0.9681	0.9853
	LPIPS↓	0.2475	0.1316	0.1681	0.0978	0.1770	0.1067

TABLE IV
CHAMFER DISTANCE (mm) FROM POINT CLOUD EXTRACTED FROM CT
ON A REAL X-RAY DATASET.

Scene	1 SDF hash	1 SDF freq	2 SDF hash	2 SDF freq
Skin↓	2.36	0.34	2.73	0.37
Bone↓	-	-	0.42	0.67
Skin↓	1.46	0.69	3.76	0.56
Bone↓	-	-	1.29	1.53

[5] M. Amirian, D. Barco, I. Herzig, and F.-P. Schilling, "Artifact reduction in 3d and 4d cone-beam computed tomography images with deep learning: a review," *IEEE Access*, vol. 12, pp. 10281–10295, 2024.

[6] R. Zha, Y. Zhang, and H. Li, "Naf: neural attenuation fields for sparse-view cbct reconstruction," in *International Conference on Medical Image Computing and Computer-Assisted Intervention*. Springer, 2022, pp. 442–452.

[7] D. Rückert, Y. Wang, R. Li, R. Idoughi, and W. Heidrich, "Neat: Neural adaptive tomography," *ACM Transactions on Graphics (TOG)*, vol. 41, no. 4, pp. 1–13, 2022.

[8] Y. Fang, L. Mei, C. Li, Y. Liu, W. Wang, Z. Cui, and D. Shen, "Snaf: Sparse-view cbct reconstruction with neural attenuation fields," *arXiv preprint arXiv:2211.17048*, 2022.

[9] Y. Cai, J. Wang, A. Yuille, Z. Zhou, and A. Wang, "Structure-aware sparse-view x-ray 3d reconstruction," in *CVPR*, 2024.

[10] B. Mildenhall, P. P. Srinivasan, M. Tancik, J. T. Barron, R. Ramamoorthi, and R. Ng, "Nerf: Representing scenes as neural radiance fields for view synthesis," in *ECCV*, 2020.

[11] Z. Shuyi, X. Shuxiang, I. Ryoichi, S. Ken, O. Masaki, and O. Takeshi, "Inf: Implicit neural fusion for lidar and camera," 2023.

[12] B. Kerbl, G. Kopanas, T. Leimkühler, and G. Drettakis, "3d gaussian splatting for real-time radiance field rendering," *ACM Transactions on Graphics*, vol. 42, no. 4, July 2023. [Online]. Available: <https://repo-sam.inria.fr/fungraph/3d-gaussian-splatting/>

[13] P. Wang, L. Liu, Y. Liu, C. Theobalt, T. Komura, and W. Wang, "Neus:

Learning neural implicit surfaces by volume rendering for multi-view reconstruction," *arXiv preprint arXiv:2106.10689*, 2021.

[14] C. J. F. Reyneke, M. Lüthi, V. Burdin, T. S. Douglas, T. Vetter, and T. E. M. Mutsvangwa, "Review of 2-d/3-d reconstruction using statistical shape and intensity models and x-ray image synthesis: Toward a unified framework," *IEEE Reviews in Biomedical Engineering*, vol. 12, pp. 269–286, 2019.

[15] G. Zheng, "Reconstruction of patient-specific 3d bone model from biplanar x-ray images and point distribution models," in *2006 International Conference on Image Processing*, 2006, pp. 1197–1200.

[16] S. Kadoury, F. Cheriet, and H. Labelle, "Personalized x-ray 3-d reconstruction of the scoliotic spine from hybrid statistical and image-based models," *IEEE Transactions on Medical Imaging*, vol. 28, no. 9, pp. 1422–1435, 2009.

[17] N. Baka, B. Kaptein, M. de Bruijne, T. van Walsum, J. Giphart, W. Niessen, and B. Lelieveldt, "2d–3d shape reconstruction of the distal femur from stereo x-ray imaging using statistical shape models," *Medical Image Analysis*, vol. 15, no. 6, pp. 840–850, 2011.

[18] H. Lamecker, T. H. Wenckebach, and H.-C. Hege, "Atlas-based 3d-shape reconstruction from x-ray images," in *18th International Conference on Pattern Recognition (ICPR'06)*, vol. 1. IEEE, 2006, pp. 371–374.

[19] T. J. Tchinde Fotsin, C. Vázquez, T. Cresson, and J. De Guise, "Shape, pose and density statistical model for 3d reconstruction of articulated structures from x-ray images," in *2019 41st Annual International Conference of the IEEE Engineering in Medicine and Biology Society (EMBC)*, 2019, pp. 2748–2751.

[20] M. Ehlke, H. Ramm, H. Lamecker, H.-C. Hege, and S. Zachow, "Fast generation of virtual x-ray images for reconstruction of 3d anatomy," *IEEE transactions on visualization and computer graphics*, vol. 19, no. 12, pp. 2673–2682, 2013.

[21] H. Kim, K. Lee, D. Lee, and N. Baek, "3d reconstruction of leg bones from x-ray images using cnn-based feature analysis," in *2019 International Conference on Information and Communication Technology Convergence (ICTC)*, 2019, pp. 669–672.

[22] B. Aubert, C. Vazquez, T. Cresson, S. Parent, and J. A. de Guise, "Toward automated 3d spine reconstruction from biplanar radiographs

- using cnn for statistical spine model fitting,” *IEEE Transactions on Medical Imaging*, vol. 38, no. 12, pp. 2796–2806, 2019.
- [23] F. Tong, M. Nakao, S. Wu, M. Nakamura, and T. Matsuda, “X-ray2shape: Reconstruction of 3d liver shape from a single 2d projection image,” in *Engineering in Medicine Biology Society (EMBC)*, 2020, pp. 1608–1611.
- [24] Y. Kasten, D. Doktofsky, and I. Kovler, “End-to-end convolutional neural network for 3d reconstruction of knee bones from bi-planar x-ray images,” 2020.
- [25] K. Sohan and M. A. Yousuf, “3d bone shape reconstruction from 2d x-ray images using med generative adversarial network,” in *2020 2nd International Conference on Advanced Information and Communication Technology (ICAICT)*, 2020, pp. 53–58.
- [26] Q. Xu, Z. Xu, J. Philip, S. Bi, Z. Shu, K. Sunkavalli, and U. Neumann, “Point-nerf: Point-based neural radiance fields,” in *Proceedings of the IEEE/CVF Conference on Computer Vision and Pattern Recognition*, 2022, pp. 5438–5448.
- [27] A. Chen, Z. Xu, A. Geiger, J. Yu, and H. Su, “Tensorf: Tensorial radiance fields,” in *European Conference on Computer Vision*. Springer, 2022, pp. 333–350.
- [28] T. Müller, A. Evans, C. Schied, and A. Keller, “Instant neural graphics primitives with a multiresolution hash encoding,” *ACM Transactions on Graphics (ToG)*, vol. 41, no. 4, pp. 1–15, 2022.
- [29] S. Fridovich-Keil, A. Yu, M. Tancik, Q. Chen, B. Recht, and A. Kanazawa, “Plenoxels: Radiance fields without neural networks,” in *Proceedings of the IEEE/CVF Conference on Computer Vision and Pattern Recognition*, 2022, pp. 5501–5510.
- [30] M. Oechsle, S. Peng, and A. Geiger, “Unisurf: Unifying neural implicit surfaces and radiance fields for multi-view reconstruction,” in *Proceedings of the IEEE/CVF International Conference on Computer Vision*, 2021, pp. 5589–5599.
- [31] Y. Wang, Q. Han, M. Habermann, K. Daniilidis, C. Theobalt, and L. Liu, “Neus2: Fast learning of neural implicit surfaces for multi-view reconstruction,” in *Proceedings of the IEEE/CVF International Conference on Computer Vision*, 2023, pp. 3295–3306.
- [32] C.-H. Lin, W.-C. Ma, A. Torralba, and S. Lucey, “Barf: Bundle-adjusting neural radiance fields,” in *Proceedings of the IEEE/CVF International Conference on Computer Vision*, 2021, pp. 5741–5751.
- [33] Y. Jeong, S. Ahn, C. Choy, A. Anandkumar, M. Cho, and J. Park, “Self-calibrating neural radiance fields,” in *2021 IEEE/CVF International Conference on Computer Vision (ICCV)*, 2021, pp. 5826–5834.
- [34] K. Schwarz, Y. Liao, M. Niemeyer, and A. Geiger, “Graf: Generative radiance fields for 3d-aware image synthesis,” in *Advances in Neural Information Processing Systems (NeurIPS)*, 2020.
- [35] W. Bian, Z. Wang, K. Li, J.-W. Bian, and V. A. Prisacariu, “Nope-nerf: Optimising neural radiance field with no pose prior,” in *Proceedings of the IEEE/CVF Conference on Computer Vision and Pattern Recognition*, 2023, pp. 4160–4169.
- [36] S. D. Roth, “Ray casting for modeling solids,” *Computer graphics and image processing*, vol. 18, no. 2, pp. 109–144, 1982.
- [37] N. Rahaman, A. Baratin, D. Arpit, F. Draxler, M. Lin, F. Hamprecht, Y. Bengio, and A. Courville, “On the spectral bias of neural networks,” in *International Conference on Machine Learning*. PMLR, 2019, pp. 5301–5310.
- [38] N. Max, “Optical models for direct volume rendering,” *IEEE Transactions on Visualization and Computer Graphics*, vol. 1, no. 2, pp. 99–108, 1995.
- [39] A. Gropp, L. Yariv, N. Haim, M. Atzmon, and Y. Lipman, “Implicit geometric regularization for learning shapes,” *arXiv preprint arXiv:2002.10099*, 2020.
- [40] J. Yang, M. Pavone, and Y. Wang, “Freenerf: Improving few-shot neural rendering with free frequency regularization,” in *Proceedings of the IEEE/CVF Conference on Computer Vision and Pattern Recognition*, 2023, pp. 8254–8263.
- [41] Z. Li, T. Müller, A. Evans, R. H. Taylor, M. Unberath, M.-Y. Liu, and C.-H. Lin, “Neuralangelo: High-fidelity neural surface reconstruction,” in *Proceedings of the IEEE/CVF Conference on Computer Vision and Pattern Recognition*, 2023, pp. 8456–8465.
- [42] S. Xie, S. Zhou, K. Sakurada, R. Ishikawa, M. Onishi, and T. Oishi, “G2fr: Frequency regularization in grid-based feature encoding neural radiance fields,” in *European Conference on Computer Vision*. Springer, 2024, pp. 186–203.
- [43] F. P. Vidal and P.-F. Villard, “Development and validation of real-time simulation of x-ray imaging with respiratory motion,” *Computerized Medical Imaging and Graphics*, vol. 49, pp. 1–15, Apr. 2016.
- [44] R. Zha, T. J. Lin, Y. Cai, J. Cao, Y. Zhang, and H. Li, “R2-gaussian: Rectifying radiative gaussian splatting for tomographic reconstruction,” in *NeurIPS*, 2024.
- [45] C. Pinter, A. Lasso, and G. Fichtinger, “Polymorph segmentation representation for medical image computing,” *Computer methods and programs in biomedicine*, vol. 171, pp. 19–26, 2019.
- [46] A. Fedorov, R. Beichel, J. Kalpathy-Cramer, J. Finet, J.-C. Fillion-Robin, S. Pujol, C. Bauer, D. Jennings, F. Fennessy, M. Sonka *et al.*, “3d slicer as an image computing platform for the quantitative imaging network,” *Magnetic resonance imaging*, vol. 30, no. 9, pp. 1323–1341, 2012.
- [47] S. Umeyama, “Least-squares estimation of transformation parameters between two point patterns,” *IEEE Transactions on Pattern Analysis & Machine Intelligence*, vol. 13, no. 04, pp. 376–380, 1991.